CRYSTAL GROWTH & DESIGN

pubs.acs.org/crystal

Article

Influence of 3d Transition Metal Impurities on Garnet Scintillator Afterglow

Vasilii M. Khanin,* Ivan Venevtsev, Kirill Chernenko, Tansu Tukhvatulina, Piotr A. Rodnyi, Sandra Spoor, Jack Boerekamp, Anne-Marie van Dongen, Daniela Buettner, Herfried Wieczorek, Cees R. Ronda, Tim Senden, and Andries Meijerink

Cite This: *Cryst. Growth Des.* 2020, 20, 3007−3017

Read Online

ACCESS | Metrics & More | Article Recommendations

ABSTRACT: Garnet scintillators often suffer from undesired afterglow, the origin of which is not always well-understood. A possible origin is contamination with transition metal (TM) ions. These impurities can act as traps giving rise to afterglow. Alternatively, they may show long-lived (microsecond) d−d emission. Here we present a systematic study on the role of 3d TM impurities in $(Lu,Gd)_3(Ga,Al)_5O_{12}$ garnet scintillators. Scintillator disks intentionally doped with ppm levels of Ti, V, Cr, Mn, Fe, Co, Ni, Cu, or Zn were studied to identify TM-related traps in thermoluminescence (TSL) glow curves and their role in afterglow. For Ti, V, and Cr additional TSL peaks were observed that gave rise to RT afterglow in the 10^{-2}−10^{3} s time range, depending on garnet composition. On the millisecond time scale long-lived red/near-infrared emission was observed from Mn and Fe impurities, explained by spin-forbidden d−d emission. We show that afterglow can be reduced by the use of ultrapure raw materials. Other solutions include bandgap engineering for the garnet host to modify trap depths and applying optical filters to block the spin-forbidden d−d emission. The present study provides an insightful overview of the role of 3d TM impurities on afterglow in Ce-doped scintillators and procedures to predict and reduce afterglow. These insights will aid the development of Ce-doped garnets with superior afterglow behavior.

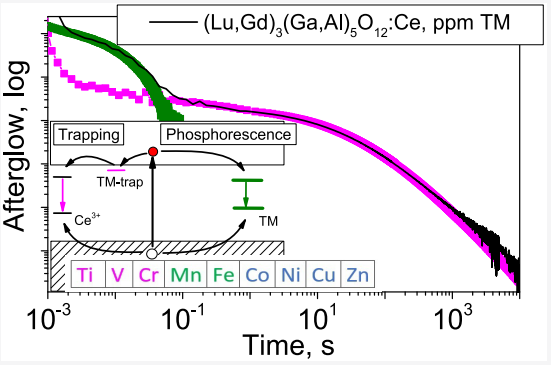

INTRODUCTION

Multicomponent Ce-doped garnets are promising luminescent materials for application in medical imaging as scintillators[1] and in lighting solutions as LED[2] or storage phosphors.[3] The main advantage of garnets lies in the ability to modify their luminescence properties, such as emission spectral range, light yield, decay, and afterglow performance through the variation of composition. The Ce^{3+} emission color is sensitive to subtle changes in the local crystal field and covalency while afterglow characteristics can be tailored by the so-called band gap engineering approach.[4] As such $(Lu,Gd)_3(Al,Ga)_5O_{12}$:Ce crystals show excellent scintillator performance[5,6] with >40 ph/keV light yield and a fast decay of 60−80 ns, while $Y_3Al_{5-y}Ga_yO_{12}$:Ce ceramics co-doped with Cr^{3+} ions are novel persistent phosphors.[7]

The performance of garnet materials can also be modified using defect engineering.[8] Single-crystal films of LuAG:Ce exhibit significantly faster decay kinetics (less afterglow) compared to single crystals or ceramics,[9] which is mainly attributed to the low sintering temperature for films during the manufacturing process which limits the formation of antisite defects.[10] There is also a strong influence of stoichiometry variations[11,12] and post-treatments in various atmospheres[13] on afterglow, transparency, and light yield. The observed effects are explained by varying concentrations of intrinsic defects[14,15] or by competition between $Ce^{3+/4+}$ ions and the traps for capture of charge carriers.[16]

Luminescence properties of garnets are influenced not only by intrinsic defects but also by trace amounts of impurities[17−19] and co-doping.[20] It has been shown that the rise time of a scintillation flash is improved by co-doping with 1000 ppm of Mg^{2+} in GGAG:Ce,Mg.[21] This can be explained by the formation of Ce^{4+} as charge compensation for Mg^{2+} on a Al^{3+} site. Ce^{4+} acts as a recombination center for conduction band (CB) electrons generated under X-ray irradiation. A higher Ce^{4+} concentration leads to faster capture and a shorter rise time of the Ce^{3+} emission that follows electron capture. Variations in X-ray excited luminescence (XRL) intensity, photoluminescence (PL) decay curves and reflection spectra of

Received: December 12, 2019
Revised: April 8, 2020
Published: April 8, 2020

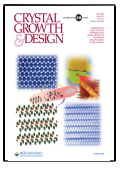

$Gd_3Ga_3Al_2O_{12}$:Ce pellets were shown to be affected by co-doping with B, Ca, Ba Mg, Sr, Zr, Fe, Bi, Zn, Ag, Nb, Cu, K, and Na ions.[22]

Raw material batches, crucible/oven materials, fluxes, and binders are sources of impurities in garnet materials. Traces of various ions are known to impact garnet scintillator efficiency, due to energy transfer (ET) to or from Ce^{3+} and also to other effects.[23−27] The role of trace TM impurities, in particular of 3d-elements, in the garnet luminescence process is important but much less studied.

In this work, we focus on $LuGd_2(Ga,Al)_5O_{12}$ multi-component garnets because of their potential as scintillators for medical imaging.[28] We systematically study the role of transition metal (TM) impurities on the afterglow behavior. Afterglow is an undesired phenomenon in scintillator materials, especially for computed tomography (CT) and positron emission tomography (PET), where afterglow gives rise to ghost images and slow response times. TM ions (especially 3d elements) are present in trace amounts in $(LuGd_2)$, $(Ga,Al)_5O_{12}$ garnet lattice due to their chemical similarity to Ga and Al ions. To systematically investigate the effect of TM ions on the afterglow behavior, we have introduced nearly all 3d TM ions into $(LuGd_2)$,$(Ga_xAl_{5-x})O_{12}$:Ce,TM in 1−100 weight ppm concentrations as TM−oxides. To study and understand the influence we measured both thermoluminescence glow curves and afterglow at room temperature (RT). These studies provide information on charge trapping and afterglow as a result of charge detrapping followed by recombination and slow phosphorescence afterglow from luminescent impurities.

EXPERIMENTAL SECTION

Ceramic garnet samples for this study were prepared at Philips Research Eindhoven by sintering a mixture of base oxides of (4N-6N)-purity in air atmosphere in the form of disks of 14 mm diameter and 1 mm thickness. $LuGd_2Ga_3Al_2O_{12}$:Ce and $LuGd_2Ga_2Al_3O_{12}$:Ce compositions were sintered with 0.2 mol % (mol %) Ce and co-doped with TM ions as 1−100 wt.ppm of TiO_2, V_2O_5, Cr_2O_3, MnO, Fe_2O_3, CoO, NiO, CuO, or ZnO, see Table 1. Table 1 also provides the translation of weight ppm (wt.ppm) of oxides into mole ppm (mol.ppm) of 3d-ions (relative to Al 0 +Ga), which is about a factor of 2−3. On the basis of the X-ray diffraction patterns, it was concluded that all samples consist of a single garnet phase. We had no means to check how well the TM co-dopants were incorporated in the garnet lattice, but it is well-known that TM-ions substitute well for both Ga^{3+} and Al^{3+}.

TSL glow curves were measured in the 80−550 K temperature range after irradiation of the samples with X-rays (55 kV, 10 mA) at 80 K. The irradiation lasted for 5 min; the samples were positioned 3 cm away from the tube. The detector was a Hamamatsu R6357 PMT, sensitive in the range of 200−900 nm. The samples were glued to the heating element with Leitsilber-200 paint to ensure good thermal contact. The waiting time between irradiation of the samples and the start of the measurements was fixed at 10 min. All the TSL curves shown in this paper were recorded with β = 15 K/min heating rate.

Afterglow curves were measured at 300 K after 6 s of irradiation with X-rays (120 kV, 100 mA, 20 cm distance) and detected with a Hamamatsu silicon photodiode and a picoammeter Keithley M6485. The curves were recorded separately in the 1 ms to 10 s and 1−2000 s time ranges and were normalized to the XRL intensity. The afterglow was measured relative to the signal level during the X-ray excitation pulse. XRL spectra were measured under continuous X-ray (40 kV, 10 mA, 3 cm distance) excitation. Emission spectra were registered in a reflection geometry using a Lomo Photonica MDR-2 monochromator (0.3 nm resolution) coupled to a Hamamatsu H8259-01 photon counting head. The spectra were corrected for wavelength dependent transmission of the monochromator and the spectral sensitivity of the PMT. XRL decay kinetics were measured after pulsed 100 ns excitation using a tungsten anode X-ray tube with a grid (0.7 A, 40 kV). The signal was acquired with Philips XQ2020 PMT and oscilloscope Tektronix 120 MHz.

Photoluminescence emission (PL) and excitation (PLE) spectra were obtained with an UC-920 Edinburg Instruments spectrofluorometer. The operating ranges of the spectrometer's excitation and emission were 250−650 and 400−700 nm, respectively. The resolution was set at 1 nm or at 0.1 nm, depending on the precision required. The equipment was calibrated to correct for the sensitivity of the monochromators and PMTs, and excitation spectra were corrected for the Xe-lamp spectrum. Cathodoluminescence (CL) spectra under 10 keV electron beam excitation on 1 mm^2 spots were recorded with a scanning electron microscope (SEM) coupled with an optical fiber to an Ocean Optics QE65000 USB-spectrometer. The spectral response of this setup was calibrated with a halogen lamp.

Table 1. List of Co-dopants Concentration in wt.ppm for oxides and mol.ppm (Relative to Al + Ga Ions) for $LuGd_2Ga_2Al_3O_{12}$:Ce (Named Ga 2) and $LuGd_2Ga_3Al_2O_{12}$:Ce (Named Ga 3) Garnet Ceramics[a]

dopant	Ga 2			Ga 3		
	wt.ppm oxide	mol.ppm ions	LY*, %	wt.ppm oxide	mol.ppm ions	LY*, %
- (Ref)	-	-	96	-	-	80
Ti				25	59	69
V	5	9.9	89	25	51.9	76
	10	19.8	90			
Cr	2	4.7	87	25	62.2	67
	10	23.8	88			
Mn	1	2.5	79	25	66.5	78
	5	12.7	80			
Fe	1	2.3	80	25	59	67
	5	11.3	73	100	236.3	47
Co	5	12	62			
Ni	5	12.1	86	25	105	82
Cu				25	98.4	77
Zn				25	97.2	68

[a]Light yield (LY) values are provided for each sample in % relative to commercial GOS:Pr as a reference (~40 photons/keV). *Pulse-height spectra for determining the LY were measured under irradiation with a ^{241}Am γ-source and detected with Hamamatsu R1104 PMT.

RESULTS AND DISCUSSION

I. TSL and Afterglow of Garnets with TM Impurities.

We start our investigations into the TM influence on garnets scintillation properties with a description of TSL and afterglow curves for $LuGd_2Ga_3Al_2O_{12}$:Ce composition co-doped with various TM ions at ppm levels. The TSL curves are analyzed to assign specific TM ions to peaks observed in the TSL spectra. This information is subsequently used to explain differences in afterglow intensities and variations in afterglow time scales at room temperature.

I.A. Correlation of TSL and Afterglow Curves. TSL glow curves measured for $LuGd_2Ga_3Al_2O_{12}$:Ce,TM are presented in Figure 1a. The reference TSL glow curve for $LuGd_2Ga_3Al_2O_{12}$:Ce ceramics (with no intentional co-dopants) is shown in Figure 1a, curve 1. The curve has a complex structure and consists of several TSL peaks: at 120, 250, 303, and 390 K. The 120 K peak is actually the high-temperature shoulder of a broad TSL structure in the range of 10−150 K,[29] beyond the limits of our measurements. These low-temperature TSL peaks are generally related to the presence of structural defects,[14] that form shallow electron

https://dx.doi.org/10.1021/acs.cgd.9b01660
Cryst. Growth Des. 2020, 20, 3007−3017

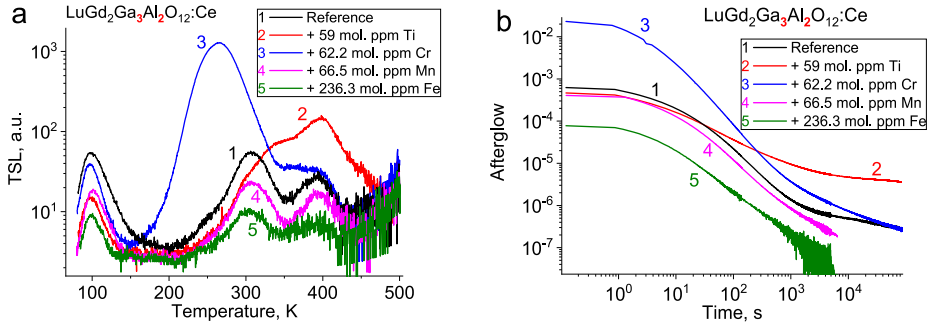

Figure 1. (a) TSL glow curves for X-ray irradiated $LuGd_2Ga_3Al_2O_{12}$:Ce,TM garnet ceramics, where TM = Ti, Cr, Mn, and Fe, and (b) RT afterglow curves measured at RT for $LuGd_2Ga_3Al_2O_{12}$:Ce,TM.

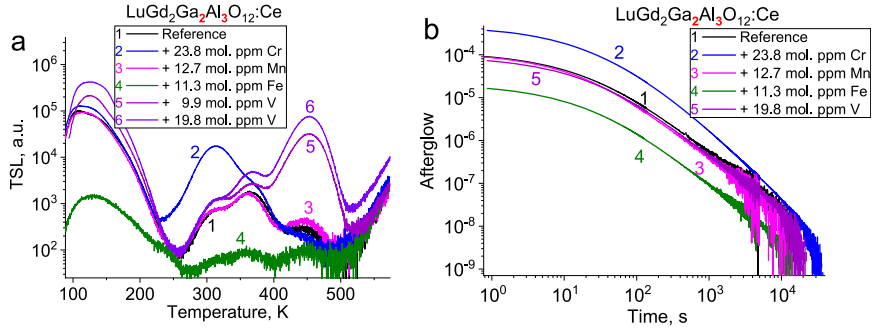

Figure 2. (a) TSL glow curves for X-ray irradiated $LuGd_2Ga_2Al_3O_{12}$:Ce,TM garnet ceramics, co-doped with 10 wt.ppm of Cr_2O_3 and 5 wt.ppm Mn, Fe, V oxides. (b) RT afterglow curves measured at RT for $LuGd_2Ga_2Al_3O_{12}$:Ce,TM (same as for part a).

traps just below the conduction band edge.[4] For the present study, these shallow traps are not the focus as the RT afterglow related to these shallow traps will be fast. In ref 30, we have shown that the 300 K TSL peak for $Gd_3Ga_3Al_2O_{12}$:Ce composition is associated Yb-impurities and the peak position barely shifts with Gd/Lu variation if the Ga content is set to 60% (Ga 3). It has been reported for various oxide garnets[31,32] that the two other TSL peaks (one on either side of the Yb-related one) are due to Cr (256 K for $LuGd_2Ga_3Al_2O_{12}$:Ce) and Ti or V (390 K) trace impurities.

The TSL glow curves for the co-doped $LuGd_2Ga_3Al_2O_{12}$:Ce,TM samples (Figure 1a) show that Ti and Cr doping leads to increased intensity of specific TSL peaks. For the $LuGd_2Ga_3Al_2O_{12}$:Ce composition, the Ti-related and Cr-related TSL peaks are located at 390 K (curve 2) and 255 K (curve 3), respectively. This is consistent with data reported in ref 31, if the shift of conduction band with composition variation is taken into account.[33] Co-doping with 25 wt.ppm of MnO (curve 4) and 100 wt.ppm of Fe_2O_3 (curve 5) oxides results in a drop of overall TSL glow curve intensity. Co-doping with V, Ni, Cu, and Zn oxides has no significant influence on the TSL glow curves (not shown for clarity of the rest of the data). This can be because of poor incorporation of these TM ions or because incorporation of these TM ions does not result in traps that interfere with the trapping and detrapping that determines the afterglow behavior.

Afterglow curves for $LuGd_2Ga_3Al_2O_{12}$:Ce,TM are shown in Figure 1b. The curves show a stronger afterglow for the Cr co-doping garnet, while the afterglow is weaker for the Mn and Fe co-doped materials. The Ti co-doped garnet shows a stronger afterglow in the long time regime (>30 s). These variations fully correlate with TSL data (Figure 1a). In our previous work we have shown that for garnets the traps responsible for afterglow in the $1-10^4$ s time scale are those that give rise to peaks in the TSL glow curve at around 200−400 K (measured with 0.25 K/s heating rate).[34] For example, the extra signal in afterglow curve of Cr-doped sample (curve 3, Figure 1b) in the $1-10^3$ s range is due to Cr-related TSL peak at 255 K (curve 3, Figure 1a).[34] The stronger slow afterglow tail ($t > 10^2$ s) for the Ti-doped sample (curve 2, Figure 1b) is consistent with the Ti-related TSL peak at 390 K (curve 2, Figure 1a). Moreover, the low overall intensity of TSL glow curves for Mn and Fe doped samples (curve 4 and 5, Figure 1a) is in agreement with a proportionally lower afterglow signal (curves 4 and 5, Figure 1b).

TSL and afterglow curves were also measured for $LuGd_2Ga_2Al_3O_{12}$:Ce,TM ceramics with a different Ga/Al ratio (Ga2−Al3). The results are shown in Figure 2. Here, not the full set of TM co-dopants was studied, only V, Cr, Mn, Fe, Co, and Ni co-doped materials were investigated. Again for TSL, in the reference (curve 1, Figure 2a) we can distinguish a broad TSL structure in the low-temperature region and three TSL peaks at higher temperatures: 315, 365, and 440 K. All the peak are shifted by ∼50 K to higher temperature as compared with $LuGd_2Ga_3Al_2O_{12}$:Ce reference (Figure 1a, curve 1) as a result of a shift of the conduction band edge to higher energies because of replacement of Ga by Al.[33] Co-doping with Cr and V leads to appearance of high-intensity TSL peaks at 315 and 460 K, respectively. Increasing the V co-doping concentration by a factor of 2 gives rise to a proportional increase of the 460 K peak (curves 5 and 6). Co, Ni (not shown), and Mn co-doping shows no visible effects on the TSL glow curves; addition of Fe results in the drop of TSL intensity by more than an order in magnitude (curve 4).

Room temperature afterglow curves for $LuGd_2Ga_3Al_2O_{12}$:Ce,TM shown in Figure 2b are consistent with the TSL data in Figure 2a. Cr co-doping leads to increased intensity of afterglow in the $1-10^3$ s range without

https://dx.doi.org/10.1021/acs.cgd.9b01660
Cryst. Growth Des. 2020, 20, 3007−3017

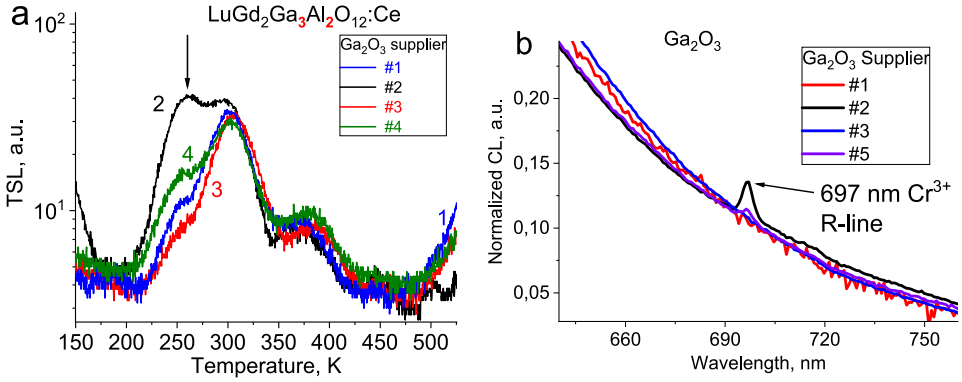

Figure 3. (a) TSL curves of $LuGd_2Ga_3Al_2O_{12}$:0.2%Ce garnet ceramics prepared with Ga_2O_3 from different sources (see Table 2). (b) RT CL spectra of Ga_2O_3 batches from different suppliers, showing Cr^{3+} R-line emission.

modification of the shape of its decay (compare curves 1 and 2, Figure 2b). From this, we conclude that afterglow in the $1-10^3$ s range is mainly due to release of charge carriers from Cr-related traps. The low overall intensity of TSL glow curve for Fe-doped samples (curve 4, Figure 2a) translates into a proportionally lower afterglow signal (curve 4, Figure 2b). Co-doping with V ions has not changed the afterglow curve shape in $1-10^4$ s range. The position of the V-related TSL peak at 460 K indicates that the V-related traps are deep traps, too deep to give rise to measurable afterglow at RT in the measured time range.

I.B. Influence of Cr Impurities on TSL. The results described in the previous section reveal that an important contribution to the RT afterglow in the Ce-doped garnets is related to Cr-impurities. To further investigate the relation between the Cr concentration and the intensity of TSL peaks and afterglow, we studied a variety of garnets synthesized using raw materials from different suppliers. According to the suppliers' lists of impurities, trace amounts of Cr ions are present in Ga_2O_3, Gd_2O_3, and Al_2O_3 starting materials. In Figure 3a, the TSL curves are shown for four samples of $LuGd_2Ga_3Al_2O_{12}$:Ce ceramics of the same composition and sintering procedure but prepared using different raw materials batches of Ga_2O_3. The TSL curves in Figure 3a show a similar overall shape of the TSL curves but with a strong variation in the intensity of the 255 K TSL peak. This is the TSL peak that was shown to be related to Cr-related traps and its intensity varies by an order of magnitude depending on the selected raw materials (Ga_2O_3) supplier.

In Table 2, we have gathered the information on the Cr trace impurity concentrations available from the supplier list. The estimations of the trace impurity content obtained from the supplier lists are of a more qualitative nature and usually give upper limits for impurity contents (e.g., "< 1 ppm"). To obtain more reliable insight in the variations in Cr-concentrations in the different Ga_2O_3 batches, cathodoluminescence (CL) measurements have been conducted. Figure 3b shows the red part of CL emission spectra of Ga_2O_3 powders from various vendors (all having similar morphology). One can see the long-wavelength part of a broad defect band emission peaking around 500 nm.[35] The main difference in the emission spectra shown in Figure 3b is the intensity of a sharp emission line around 697 nm. This emission line is characteristic of the $Cr^{3+2}E$-$^4A_2$ emission and known as R-line emission.[36] Ga_2O_3 from suppliers #2 and #5 show a clear Cr^{3+} emission peak at 697 nm, while the other Ga_2O_3 batches exhibit no visible emission lines in the area. The relative intensity of the R-line emission is about 4 times higher for Ga_2O_3 from supplier #2 than Ga_2O_3 from supplier #5. The use of Ga_2O_3 from supplier #2 for $LuGd_2Ga_3Al_2O_{12}$:Ce ceramics synthesis leads to the highest TSL peak intensity at 255 K (curve 1 Figure 3a) compared to the use of other Ga_2O_3 batches (Figure 3a). The intensity ratio of 3:1 for the TSL peak intensity for garnets made using Ga_2O_3 from supplier #2 vs supplier #5 is close to the ratio of 4:1 for the R-line intensities for Ga_2O_3 from these suppliers. For various Al_2O_3 oxide batches we have observed the same correlations between Cr-impurity contents from supplier lists, CL measurements of raw materials, and TSL intensities of garnet glow curves (not shown for briefness).

Table 2. Correlation of Cr-Impurity Contents from Supplier Lists (ppm), Intensities of Cr-Related TSL Peaks (au) and Cr^{3+} R-Line Emission CL Intensities (au)

supplier	Ga_2O_3 Cr trace, ppm	TSL intensity, 255 K, au	CL intensity for Cr, au
#1	<0.05	8.6	0
#2	0.96	37.9	26.1
#3	<0.01	5.2	0
#4	no data	12.7	not measured
#5	<0.01	12.5	6.4

In order to validate our findings about the influence of Cr-trace impurity on TSL and afterglow curves of garnets and further quantify the role of Cr-impurities on the afterglow, we co-doped $LuGd_2Ga_2Al_3O_{12}$:Ce ceramics with 4.7 and 23.8 mol.ppm of Cr ions. The TSL and afterglow curves are shown in Figure 4. In the $LuGd_2Ga_2Al_3O_{12}$:Ce (Ga 2) composition, the TSL peak related to Cr impurity is located at 315 K (Figure 4a). This TSL peak increases in intensity proportionally to Cr co-doping concentrations.

Afterglow curves in the range of $10^{-3}-10^4$ s for $LuGd_2Ga_2Al_3O_{12}$:Ce,Cr ceramics are shown in Figure 4b. The reference curve consists of two distinct components: the $10^{-3}-10^{-1}$ s and the $10^{-1}-10^4$ s region. Co-doping with Cr ions leads to an increase of the afterglow signal in the $10^{-1}-10^4$ s time window while the shape of the curve stays the same. The afterglow intensity increase is proportional to the Cr co-doping concentration. Comparison between parts a and b of Figure 4 shows a correlation between the intensity of TSL peaks in the 250–350 K range and afterglow in the $10^{-1}-10^4$ s time window. This is consistent with previous observations in $(Y,Gd)_3Al_5O_{12}$:Ce.[34] The afterglow in the $10^{-3} - 10^{-1}$ s range

https://dx.doi.org/10.1021/acs.cgd.9b01660
Cryst. Growth Des. 2020, 20, 3007−3017

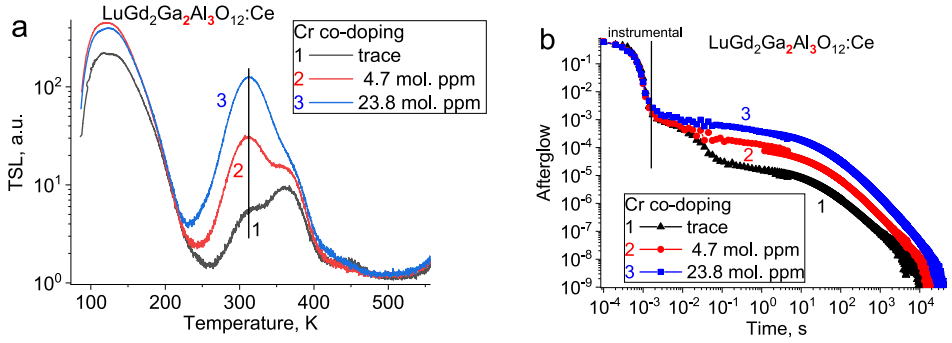

Figure 4. (a) TSL glow and (b) RT afterglow curves of $LuGd_2Ga_2Al_3O_{12}$:Ce,Cr ceramics co-doped with 0.0, 4.7, and 23.8 mol.ppm of Cr ions.

for $LuGd_2Ga_2Al_3O_{12}$:Ce (curve 1 Figure 4b) does not depend on changes in TSL glow curve caused by variations in the Cr impurity concentrations.

I.C. Impurity Concentration vs TSL Peak Intensity. To investigate the relation between the impurity concentration and the intensity of their corresponding TSL peaks, Figure 5

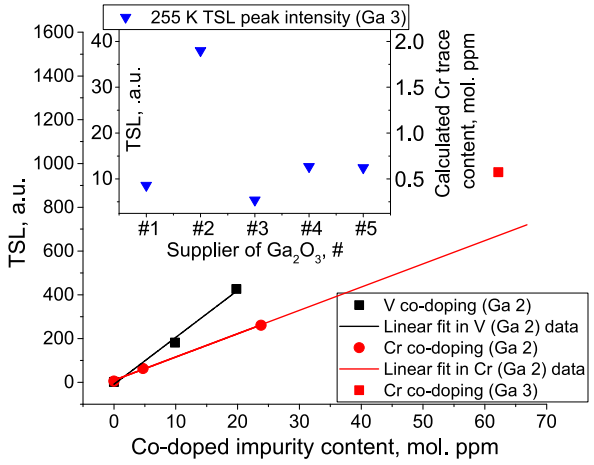

Figure 5. Dependence of specific TSL peak intensity on impurity (Cr and V) co-dopant concentration (see also Figures 2a and 4a). Inset: calculations of Cr trace impurity content depending on Ga_2O_3 supplier from the 255 K TSL glow peak intensity for $LuGd_2Ga_3Al_2O_{12}$:Ce garnet ceramics from Figure 3a.

shows the TSL peak intensities as a function of Cr (red) and V (black) concentration. The observed dependence of the TSL intensity on co-dopant concentration is close to linear, though the slope is different for V and Cr co-dopants. Differences in the capture cross-section of the V- and Cr-related traps or probability for incorporation of these ions into the garnet host lattice are possible explanations for the different slopes.

By extrapolating the TSL peak intensity of co-doped samples for the variety of samples sintered with different batches of raw materials, we can estimate the trace concentration of impurities relevant for afterglow with ±0.2 ppm precision (inset of Figure 5) The sensitivity of our TSL equipment determines the lower detection limit for TM impurity trace concentration at ~0.1 ppm. It is important to note that the consistent relation between impurity concentration and TSL signal gives rise to a reliable calibration curve for TM dopant concentrations, but the estimations are only valid for a system synthesized in the same manner and with the same annealing procedure. It is also important to realize that the proportionality of TSL peak intensity on the co-dopant (Cr, V) concentration does not explain the microscopic origin of the defect responsible for charge carrier trapping leading to the respective TSL and afterglow signal. We do not aim at elucidating the carrier capture mechanism, and therefore, in this work, we simply refer to TSL peaks associated with impurities as, e.g., "Cr-related peaks".

I.D. Reducing TSL Glow Curve Intensity. In sections I.A–I.C, we have discussed the role of impurities that give rise to additional TSL peaks, leading to a different afterglow behavior that is explained by the role of TM-related traps. There are other TM impurities that do not give rise to an extra TSL peak but affect the TSL glow curve in such a manner that all TSL peaks change their intensity. Examples have been shown in Figures 1a and 2a for co-dopants like Fe and Mn. Addition of these co-dopants leads to an overall decrease of the TSL glow curve intensity, while keeping its structure nearly the same. A similar influence on the TSL curve intensity and structure has been observed for garnets[8] and LYSO:Ce[37] co-doped with Mg^{2+} or Ca^{2+}. The effect has been explained by increased concentration of Ce^{4+}.[8,38] Addition of divalent co-dopants on Al^{3+}/Ga^{3+} sites leads to charge compensation by Ce^{4+}. The higher probability to capture electrons from CB by Ce^{4+} competes with trapping of CB electrons in electron traps.[39] For these TM-impurities, no new TM-related traps are formed, but the competition of trapping by existing traps and Ce^{4+} is altered. These effects are similar to the influence of annealing garnet materials in reducing or oxidizing atmosphere which also leads to an overall change in TSL glow curve intensity.[13] Reduced TSL intensities and improved scintillator performance was observed after treatment of garnets in oxidizing atmosphere and was interpreted as originating from oxidation of Ce^{3+} to Ce^{4+}.

The present observations suggest that Fe and Mn co-doping acts in a similar manner: these TM impurities stabilize Ce^{4+} and thus increase the probability of direct radiative recombination by trapping at Ce^{4+} compared to capture and delayed emission/TSL following electron trapping by defect/impurity traps. It is not yet clear why Ni^{2+}, Co^{2+}, Cu^{2+}, and Zn^{2+} ppm co-doping has not shown a similar effect as Fe^{2+} and Mn^{2+} (and Mg^{2+} and Ca^{2+}) of lowering the afterglow and TSL signal for garnets, either in this work or in earlier work.[22] Further work is required to investigate how different (divalent) TM-impurities can promote the formation of Ce^{4+} in garnets.

Summarizing this section, we have shown that Ti, V, or Cr co-doping leads to the appearance (or increase) of a TSL peak, unique for each impurity. The temperature maximum of the characteristic TSL peaks is affected by the Al–Ga ratio in the garnet, related to changes in the energy of the conduction band edge. The intensity of TSL peaks can be correlated with

https://dx.doi.org/10.1021/acs.cgd.9b01660
Cryst. Growth Des. 2020, 20, 3007–3017

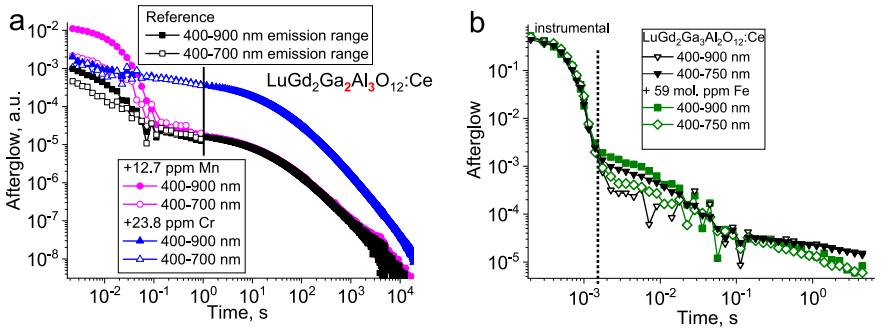

Figure 6. Afterglow curves measured at RT for (a) $LuGd_2Ga_2Al_3O_{12}$:Ce ceramics co-doped with Cr or Mn ions with and without short-pass 700 nm filter and (b) $LuGd_2Ga_3Al_2O_{12}$:Ce ceramics co-doped with Fe ions with and without short-pass 750 nm filter.

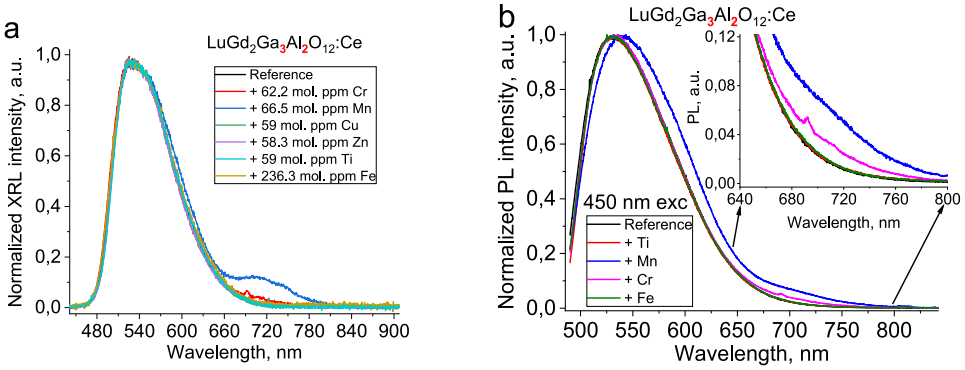

Figure 7. (a) RT XRL spectra for $LuGd_2Ga_3Al_2O_{12}$:Ce 0.2%, TM ceramics co-doped with 25 wt.ppm of Cr, Mn, Cu, Ti, Zn oxides and 100 wt.ppm Fe oxide. (b) RT PL spectra for $LuGd_2Ga_3Al_2O_{12}$:Ce 0.2%, TM ceramics co-doped with 25 wt.ppm of Cr, Mn, Fe, Ti oxides. Excitation is at 450 nm.

changes in the afterglow behavior, where especially Cr-related traps strongly increase the room temperature afterglow in the $1-10^3$ s time window. Fe and Mn co-dopants reduce the overall TSL and afterglow signal.

II. Phosphorescence of TM Impurities. In section I afterglow related to thermally stimulated release of trapped charge carriers was discussed. This is the most commonly discussed origin of afterglow. However, also slow forbidden emission from impurities can contribute to afterglow. In this section, we identify the role of spin- and parity-forbidden d−d emission of TM impurities in the afterglow of $LuGd_2Ga_2Al_3O_{12}$:Ce scintillators.

II.A. Identification of Phosphorescence in Afterglow. The origin of afterglow can be thermal detrapping of electrons followed by recombination with Ce^{4+} giving rise to delayed Ce^{3+} d−f emission. The time scale of this type of afterglow is related to the trap depth and thus the position of TSL peaks in the TSL glow curve. Alternatively, afterglow may result from phosphorescence from impurity ions. As the emission is usually detected by light detectors (photomultipliers or photodiodes) directly coupled to the scintillator, the full emission spectrum corresponding to the spectral response curve of the detector is measured. As a result, also slow (ms) emission due to spin-forbidden d−d emission in the red/infrared spectral region from TM impurities as Cr^{3+}, Mn^{2+}, Mn^{3+}, or Fe^{3+} is detected. Carrier trapping by or energy transfer from Ce^{3+} to these impurities can thus result in the observation of ms afterglow, unrelated to peaks in the TSL spectrum. To investigate the role of this type of afterglow, spectral filters can be used to filter out emission in the red or infrared. In Figure 6a the influence of a short-pass 700 nm filter on afterglow curves for $LuGd_2Ga_2Al_3O_{12}$:Ce reference sample and $LuGd_2Ga_2Al_3O_{12}$:Ce,TM co-doped with 12.7 mol.ppm of Mn or 23.8 mol.ppm of Cr ions is shown. Open dots show afterglow measured in the 400−700 nm range (with short-pass filter), while solid dots belong to afterglow measured in the 400−900 nm range (no filter).

Application of the filter to the reference sample as well as the Mn-co-doped sample leads to a reduced afterglow signal in the $10^{-2}-10^{-1}$ s range. Co-doping with Mn enhances the ms-afterglow component by an order of magnitude, while filtering out red emission from the sample decreases this afterglow component by a factor of 5. There are no visible changes in afterglow for Cr-co-doped ceramics with and without the filter. In Figure 6b we show a similar experiment with 750 nm short-pass filter applied to $LuGd_2Ga_3Al_2O_{12}$:Ce co-doped with 59 mol.ppm Fe^{3+} ions. Fe co-doping has a similar effect compared to Mn-co-doping: ms-afterglow is enhanced by co-doping and reduced by the use of short-pass red filter. The experimental results with Fe co-doping are in agreement with Nakamura et al.[40] The authors have correlated the Fe^{3+} emission band at 750−850 nm with high level of afterglow in the ms time range for $Gd_3Ga_2Al_3O_{12}$:Ce garnets. The dependence of ms-afterglow intensity on Fe^{3+} co-doping concentration was linear.[40]

From the dependence of afterglow curves on the use of short-pass filters, we can conclude that Fe and Mn ions contribute to ms-afterglow through emission that does not belong to Ce^{3+} but is the spin-forbidden d−d emission of the Fe and Mn impurities.

II.B. XRL and PL of Garnets with TM Impurities. To gain further insight into the influence of TM impurities on garnet scintillation properties in this section, we measure and discuss

https://dx.doi.org/10.1021/acs.cgd.9b01660
Cryst. Growth Des. 2020, 20, 3007−3017

X-ray luminescence (XRL) and photoluminescence (PL) spectra at room temperature for $LuGd_2Ga_3Al_2O_{12}$:Ce. In Figure 7a, the normalized XRL spectra measured at RT for $LuGd_2Ga_3Al_2O_{12}$:Ce co-doped with 25 wt.ppm of 3d transition metal oxides (except of 100 wt.ppm of Fe_2O_3) are shown. Most of the spectra are almost identical to that of the reference ceramics spectrum, and only co-doping with Cr (692 nm), Mn (620 and 710 nm), and Fe (785 nm) show extra lines or bands in the red/infrared parts of the spectra. The integral XRL intensities for each sample are proportional to the LY values provided in Table 1. A reduction in LY is observed upon addition of all TM co-dopants, also for Ti, V, Co, Ni, Cu, and Zn, which will not be discussed in this section as no extra PL bands/lines were observed for these TM dopants in $LuGd_2Ga_3Al_2O_{12}$:Ce.

Normalized PL spectra excited in the Ce^{3+} $5d_1$ band (450 nm) are shown in Figure 7b and are similar to the XRL spectra. The observation of the extra red band for Mn co-doping and 692 nm line for Cr co-doping reflects energy transfer from Ce^{3+} to these impurities, consistent with previous observations of resonant energy transfer from Ce^{3+} to Cr^{3+},[41,42] Fe^{3+},[40] and Mn^{3+}[25] ions. The relative intensities of the extra emission bands in the PL spectra is however weaker than in the XRL spectra. This shows that in addition to energy transfer from Ce^{3+} to Mn^{3+} and Cr^{3+}, also direct charge carrier recombination on the TM impurities or energy transfer via Gd^{3+} contributes to the red/infrared emission from the TM ions under X-ray excitation. The same PL spectra can be obtained with $Gd^{3+}{}^8S_{7/2} \rightarrow {}^6I_{7/2}$ f–f transitions (275 nm) excitation, confirming $Gd^{3+} \rightarrow TM^{3+}$ (TM = Cr, Mn, Fe) energy transfer (not shown for briefness).

II.C. Mn Luminescence in LGGAG:Ce, LGGAG:Mn, and LGGAG:Ce,Mn. In Figure 8, photoluminescence excitation

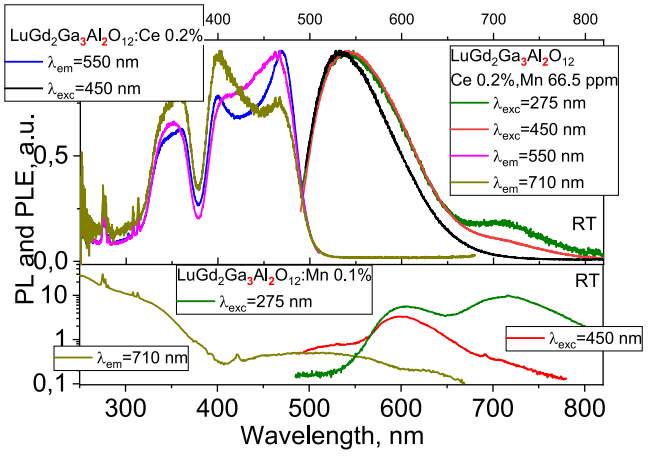

Figure 8. PLE and PL spectra of LGGAG:Ce0.2%, LGGAG:-Ce0.2%,Mn0.007% and LGGAG:Mn0.1% ceramics, measured at RT. Excitation wavelengths (for PL spectra) and emission wavelengths (for PLE spectra) are indicated in the figures.

(PLE) and emission spectra are presented for $LuGd_2Ga_3Al_2O_{12}$:Ce garnets singly doped with 0.2 mol.% Ce or 0.1 mol.% Mn and also co-doped with 0.2 mol.% Ce and 66.5 mol.ppm Mn. PL and PLE spectra of Ce^{3+} (Figure 8, top graph) show the characteristic spectra for garnets.[43] The excitation band around 450 nm ($5d_1$ band) of Ce^{3+} is strongly distorted as a result of saturation effects caused by complete absorption of the excitation light because of the high absorption strength and long path length of the excitation light in the transparent ceramic. The PL spectrum consists of a broad $5d_1$–$4f$ Ce^{3+} emission with maximum at 540 nm. The PLE spectrum consists of $4f$–$5d_1$ (450 nm) and $4f$–$5d_2$ (350 nm) Ce^{3+} bands and $^8S_{7/2} \rightarrow {}^6P_J$ and $^8S_{7/2} \rightarrow {}^6I_J$ f–f transitions of Gd^{3+} (275 and 313 nm, respectively). Gd^{3+} excitation lines are visible due to Gd → Ce energy transfer.[44]

In the co-doped $LuGd_2Ga_3Al_2O_{12}$:Ce, Mn ceramics, an extra emission band can be observed with maximum at 710 nm. Moreover, the broad emission band at 550 nm is shifted to the red as compared to the singly Ce^{3+}-doped garnet of the same composition. To understand the changes in the emission spectra for the co-doped garnet, luminescence spectra were recorded for $LuGd_2Ga_3Al_2O_{12}$:Mn, singly doped with Mn ions (Figure 8, bottom spectrum). The PL spectra show two broad bands, one around 600 nm and one around 710 nm. The relative intensity of the two bands depends on the excitation wavelength. The emission spectrum excited at 275 nm consists of two bands at 600 and 710 nm of almost equal intensity. The excitation spectrum of the 710 nm band shows $Gd^{3+}{}^8S_{7/2} \rightarrow {}^6P_J$, $^8S_{7/2} \rightarrow {}^6I_J$ lines (313 and 275 nm), a strong excitation band around 300 nm and a broad band at 500 nm. In refs 45 and 46, the Mn-related PL bands were explained by Jahn–Teller distorted $^5T_2 \rightarrow {}^5E$ (^5D) transitions of Mn^{3+} in octahedral coordination. Here we will not discuss the origin of the 620 and 710 nm emission bands in detail. Next to Mn^{3+} emission also Mn^{2+} can contribute to the 600 nm emission band.[46] It is evident that the presence of the Mn-related emission bands is consistent with the shoulder on the long wavelength side of the Ce^{3+} d–f emission band and the extra emission band around 720 nm in the Ce, Mn co-doped garnet.

To further investigate the dynamics of the Mn-related emission bands, in Figure 9 the luminescence decay of

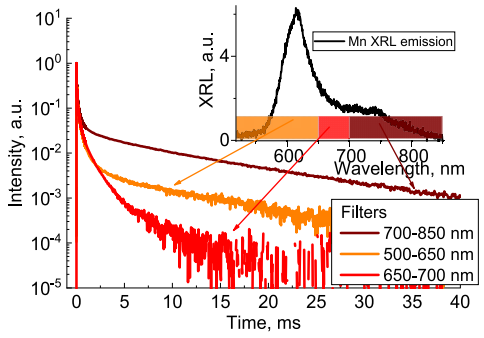

Figure 9. XRL decay kinetics at RT of $LuGd_2Al_2Ga_3O_{12}$: 0.1%Mn ceramics for specific wavelength regions selected using bandpass filters. Inset shows the filters transmittance and the XRL spectrum of $LuGd_2Al_2Ga_3O_{12}$:Mn at RT.

$LuGd_2Al_2Ga_3O_{12}$:Mn under pulsed X-ray irradiation is shown. Application of filters is used to identify the decay dynamics of different spectral components. The results show that the 500–650 nm Mn band has 77 ± 3 μs decay with a weaker 9.9 ± 0.2 ms decay component, while the 700–850 nm part of the Mn emission has a weak 77 ± 3 μs initial decay component and a stronger exponential tail with a decay time of 11.1 ± 0.1 ms. The latter value is close to the decay time (~10–14 ms) of the extra afterglow component related to Mn co-doping (Figure 6a). It is challenging to assign the various emission bands to transitions on Mn^{2+} or Mn^{3+}. Mn^{2+} can show long-lived (~10 ms) emission in the 500–650 nm spectral range resulting from

https://dx.doi.org/10.1021/acs.cgd.9b01660
Cryst. Growth Des. 2020, 20, 3007–3017

the spin-forbidden $^4T_1-^6A_1$ transition. Mn^{3+} can show spin-allowed (μs) $^5T_2-^5E$ emission or spin-forbidden $^1T_2-^5E$ emission in the red and near-infrared spectral range, depending on the crystal field splitting. Previous work in refs 45 and 46 at RT has assigned both 610 and 720 nm bands to Mn^{3+} transitions. It is beyond the scope of this paper to assign and explain the Mn-related emission bands. We can conclude that ~10 ms phosphorescence is related to Mn emission, and this significantly influences the afterglow signal in ms-time range.

II.D. Cr Luminescence in LGGAG:Ce, YAG:Cr, and LGGAG:Ce,Cr. To gain insight in the role of Cr^{3+} emission on the afterglow of garnet scintillators, luminescence spectra were measured for Ce^{3+},Cr^{3+} co-doped and singly Cr^{3+}-doped $LuGd_2Ga_3Al_2O_{12}$. The spectra in Figure 10 show the presence

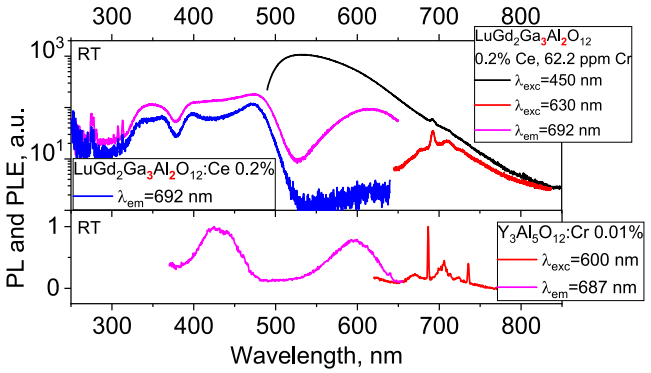

Figure 10. PLE and PL spectra of $LuGd_2Ga_3Al_2O_{12}$:Ce 0.2%, $LuGd_2Ga_3Al_2O_{12}$:Ce 0.2%, Cr 0.006%, and YAG:Cr 0.01% ceramics measured at RT. Excitation wavelengths (for PL spectra) and emission wavelengths (for PLE spectra) are indicated in the figures.

of an extra line at 692 nm in emission spectra of $LuGd_2Ga_3Al_2O_{12}$:0.2 mol.% Ce, 62.2 mol.ppm of Cr. The 692 nm line is assigned to the ^2E (^2G) → $^4A_2$(^4F) transitions of Cr^{3+}.[47] The excitation spectrum of this line consists of Ce^{3+} bands at 350 nm 450 nm, Gd^{3+} lines at 275 and 313 nm and a band at 630 nm, which can be explained by the $Cr^{3+}$$^4A_2$ → $^4T_2$ (^4F) transition. Under direct excitation of Cr^{3+} 630 nm for $LuGd_2Ga_3Al_2O_{12}$:Ce, Cr the typical R-line emission of Cr^{3+} can be clearly observed at RT. For clarity the bottom graph is added to Figure 9, depicting Cr^{3+} PL and PLE spectra for YAG:Cr (singly doped) at RT. In YAG;Cr emission occurs from the ^2E state (the lowest excited state) resulting in a sharp zero-phonon line with vibronic side bands. These spectra confirm the assignment of the sharp line emission at 692 nm to Cr^{3+} R-line emission. In Ga-containing garnets due to lower crystal field, the energy difference between ^2E state and $^4T_2$(slightly higher in energy than the ^2E level) state is small, which gives rise to a broad $^4T_2-^4A_2$ emission band with a sharp $^2E-^4A_2$ line superimposed, as observed for $LuGd_2Ga_3Al_2O_{12}$:Ce^{3+},Cr^{3+}.

The ^2E emission is spin-forbidden and has a millisecond decay time. At RT, the $^4T_2$ state is thermally populated, and a significant part of the emission is from the $^4T_2$ level which shortens the emission decay time as the $^4T_2-^4A_2$ transition is spin-allowed with a microsecond decay time. For Cr^{3+} in $LuGd_2Al_2Ga_3O_{12}$, the decay time of the mixed $^4T_2/^2E$ → $^4A_2$ emission is around 200 μs at RT.[48,49] This is too fast to be observed in our afterglow measurements.

Summarizing, in this section we have shown that even low levels of co-dopants (order of tens of mol.ppm) leads to visible photo- and X-ray luminescence of Cr^{3+},[41] Fe^{3+} (see[40]) and Mn^{3+}/Mn^{2+} ions due to energy transfer from Gd^{3+} and Ce^{3+} ions or by direct charge carrier trapping. Other co-dopants (e.g., Ni, Cu, Zn) have shown no visible effect luminescence properties of garnets (no extra emission lines/bands), but they do negatively affect the LY of samples (see Table 1).

III. Mitigating Influence of Phosphorescent Impurities. Trace amounts of TM ions are always present in raw materials used for garnet manufacturing. Moreover impurity concentrations may increase during milling and sintering procedures. Careful selection of the synthesis process and raw materials helps in reducing afterglow (including phosphorescence) levels for scintillation application of garnets. High purity starting materials are however costly and low (ppm) levels of certain TM ions cannot be prevented. In this section we show one of the potential strategies to reduce afterglow.

An alternative/additional path to reduce afterglow due to phosphorescence is the use of short-pass filters that transmit the Ce^{3+} emission and block the red/infrared phosphorescence from impurities as Mn or Fe. For a high transmittance short pass filter the Ce^{3+} emission is not influenced (except for reflection losses at filter surfaces). In Figure 11, the effect of

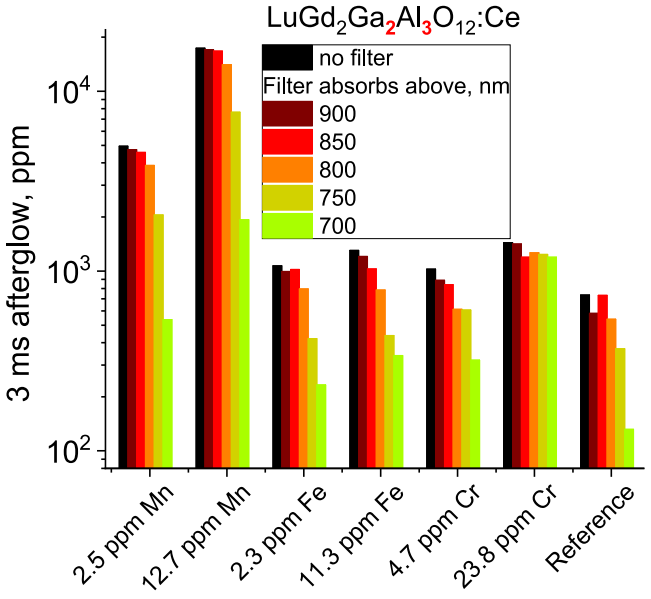

Figure 11. Afterglow measured after 3 ms for reference $LuGd_2Al_3Ga_2O_{12}$:Ce 0.2% and Mn, Fe, Cr co-doped garnet ceramics (concentrations indicated in the figure), without filters (black) and with short-pass filters that absorb light above 900 (wine), 850 (red), 800 (orange), 750 (yellow), and 700 nm (green). Note the logarithmic afterglow scale.

short-pass filters on ms-afterglow and phosphorescence of $LuGd_2Al_3Ga_2O_{12}$:Ce is shown for a variety of filters. The filters used were sprayed on glass plates and result in a ~ 20% LY loss. Filtering out long wavelength red/infrared emission without reflection losses can be realized by the choice of a detector with a suitable spectral response curve, e.g. a photomultiplier tube with a cutoff wavelength at ~700 nm.

An important measure for the influence of afterglow on image quality for CT scanners is the afterglow intensity after 3 ms. The 3 ms afterglow for reference $LuGd_2Ga_2Al_3O_{12}$:Ce ceramics shows strong influence on the filter applied between the sample and the photodetector as shown in Figure 11. The

https://dx.doi.org/10.1021/acs.cgd.9b01660
Cryst. Growth Des. 2020, 20, 3007−3017

afterglow intensity is shown (in ppm) relative to the signal level during the X-ray excitation pulse. It gradually decreases from 800 ppm down to 130 ppm with the use of 900 → 850 → 800 → 750 → 700 nm short-pass filters. Co-doping with Mn, Fe and Cr ions gives a significant rise in the 3 ms-afterglow level. For Mn and Fe co-doping the 3 ms afterglow can be effectively reduced through the application of short-pass filters. This is consistent with the observation of spin-forbidden emission with a ∼ 10 ms decay times from Mn and Fe co-dopants. The Cr-related afterglow is not reduced by application of filters. This observation is also in agreement with the analysis above where the Cr-induced afterglow was shown to originate from detrapping of electrons from Cr-related traps.

CONCLUSIONS

Transition metal impurities have a significant influence on the afterglow of garnet scintillators. Insight in the origin of the afterglow is crucial to reduce undesired afterglow. To elucidate the role of all 3d transition metals (TM), we have systematically measured thermally stimulated luminescence, room temperature afterglow, photoluminescence, and X-ray excited luminescence spectra of $LuGd_2(Al,Ga)_5O_{12}$:Ce garnets co-doped with ppm levels of various TM ions (Ti, V, Cr, Mn, Fe, Co, Ni, Cu, or Zn). Different effects were observed for TSL: some TM ions give rise to extra TSL peaks (Cr, V, Ti) while for others co-doping results in a decrease of the overall TSL intensity (Fe, Mn). Some TM-impurities (Fe, Mn, Cr) add extra spectrally resolved afterglow emission bands/lines in the red/infrared, which can also be observed in luminescence spectra. For Co, Ni, Cu, and Zn, no effect on TSL, luminescence, and afterglow of garnets was observed, except for a drop in light yield.

The extra TSL peaks observed upon co-doping with Ti, V, or Cr are assigned to TM-related electron traps. The temperature maximum of the peak can be tailored by the garnet composition (e.g., Al/Ga ratio) to change the energy of the conduction band edge. In particular, the Cr-related trap is important as it is a shallow trap that gives rise to a TSL peak close to room temperature. This results in significant RT afterglow that can be reduced by choosing high purity (low Cr content) raw materials for garnet synthesis. An additional afterglow signal observed in $(Lu,Gd)_3(Al,Gd)_5O_{12}$:Ce garnets is explained by slow (∼10 ms lifetime) spin-forbidden d−d emission of Mn and Fe impurities showing emission in the 600−800 nm range. This afterglow is shown to be strongly reduced by application of short-pass filters to block red/infrared emission.

In the present study, we provide a complete overview of the influence of ppm impurity levels of 3d TM impurities on the RT afterglow of garnet scintillators. Insight is given in the origin of the afterglow and on methods to reduce the afterglow are discussed. These insights are important in the realization of superior scintillators for medical imaging, especially for CT and PET where afterglow adversely affects image quality.

AUTHOR INFORMATION

Corresponding Author

Vasilii M. Khanin − *Utrecht University, 3584 CC Utrecht, The Netherlands;* orcid.org/0000-0001-6399-1540; Email: khanin.vasilii@mail.ru

Authors

Ivan Venevtsev − *Peter the Great St. Petersburg Polytechnic University, 195251 St. Petersburg, Russia*

Kirill Chernenko − *MAX IV Laboratory, Lund University, SE-22100 Lund, Sweden*

Tansu Tukhvatulina − *Peter the Great St. Petersburg Polytechnic University, 195251 St. Petersburg, Russia*

Piotr A. Rodnyi − *Peter the Great St. Petersburg Polytechnic University, 195251 St. Petersburg, Russia*

Sandra Spoor − *Philips Research, 5656 AE Eindhoven, The Netherlands*

Jack Boerekamp − *Philips Research, 5656 AE Eindhoven, The Netherlands*

Anne-Marie van Dongen − *Philips Research, 5656 AE Eindhoven, The Netherlands*

Daniela Buettner − *Philips Research, 5656 AE Eindhoven, The Netherlands*

Herfried Wieczorek − *Philips Research, 5656 AE Eindhoven, The Netherlands*

Cees R. Ronda − *Philips Research, 5656 AE Eindhoven, The Netherlands*

Tim Senden − *Utrecht University, 3584 CC Utrecht, The Netherlands*

Andries Meijerink − *Utrecht University, 3584 CC Utrecht, The Netherlands;* orcid.org/0000-0003-3573-9289

Complete contact information is available at: https://pubs.acs.org/10.1021/acs.cgd.9b01660

Notes

The authors declare no competing financial interest.

REFERENCES

(1) Cherepy, N. J.; Payne, S. A.; Asztalos, S. J.; Hull, G.; Kuntz, J. D.; Niedermayr, T.; Pimputkar, S.; Roberts, J. J.; Sanner, R. D.; Tillotson, T. M.; et al. Scintillators with Potential to Supersede Lanthanum Bromide. *IEEE Trans. Nucl. Sci.* **2009**, *56*, 873−880.

(2) Setlur, A. Phosphors for LED-Based Solid-State Lighting. *Electrochem. Soc. Interface* **2009**, *16*, 32.

(3) Ueda, J.; Aishima, K.; Nishiura, S.; Tanabe, S. Afterglow Luminescence in Ce3+-Doped Y3Sc2Ga3O12 Ceramics. *Appl. Phys. Express* **2011**, *4*, 042602.

(4) Fasoli, M.; Vedda, A.; Nikl, M.; Jiang, C.; Uberuaga, B. P.; Andersson, D. A.; McClellan, K. J.; Stanek, C. R. Band-Gap Engineering for Removing Shallow Traps in Rare-Earth Lu3Al5O12 Garnet Scintillators Using Ga3+ Doping. *Phys. Rev. B: Condens. Matter Mater. Phys.* **2011**, *84*, 081102.

(5) Kamada, K.; Endo, T.; Tsutumi, K.; Yanagida, T.; Fujimoto, Y.; Fukabori, A.; Yoshikawa, A.; Pejchal, J.; Nikl, M. Composition Engineering in Cerium-Doped (Lu, Gd) 3 (Ga, Al) 5O12 Single-Crystal Scintillators. *Cryst. Growth Des.* **2011**, *11*, 4484−4490.

(6) Luo, J.; Wu, Y.; Zhang, G.; Zhang, H.; Ren, G. Composition-Property Relationships in (Gd3- XLux)(GayAl5- y) O12: Ce (X= 0, 1, 2, 3 and Y= 0, 1, 2, 3, 4) Multicomponent Garnet Scintillators. *Opt. Mater. (Amsterdam, Neth.)* **2013**, *36*, 476−481.

(7) Ueda, J.; Kuroishi, K.; Tanabe, S. Bright Persistent Ceramic Phosphors of Ce3+-Cr 3+-Codoped Garnet Able to Store by Blue Light. *Appl. Phys. Lett.* **2014**, *104*, 101904.

(8) Nikl, M.; Kamada, K.; Babin, V.; Pejchal, J.; Pilarova, K.; Mihokova, E.; Beitlerova, A.; Bartosiewicz, K.; Kurosawa, S.; Yoshikawa, A. Defect Engineering in Ce-Doped Aluminum Garnet Single Crystal Scintillators. *Cryst. Growth Des.* **2014**, *14*, 4827−4833.

(9) Zorenko, Y.; Gorbenko, V.; Mihokova, E.; Nikl, M.; Nejezchleb, K.; Vedda, A.; Kolobanov, V.; Spassky, D. Single Crystalline Film Scintillators Based on Ce-and Pr-Doped Aluminium Garnets. *Radiat. Meas.* **2007**, *42*, 521−527.

https://dx.doi.org/10.1021/acs.cgd.9b01660
Cryst. Growth Des. 2020, 20, 3007−3017

(10) Nikl, M.; Mihokova, E.; Pejchal, J.; Vedda, A.; Zorenko, Y.; Nejezchleb, K. The Antisite LuAl Defect-related Trap in Lu3Al5O12: Ce Single Crystal. *Phys. Status Solidi B* **2005**, *242*, R119−R121.
(11) Kanai, T.; Satoh, M.; Miura, I. Characteristics of a Nonstoichiometric Gd3+ δ (Al, Ga) 5- ΔO12: Ce Garnet Scintillator. *J. Am. Ceram. Soc.* **2008**, *91*, 456−462.
(12) Seeley, Z. M.; Cherepy, N. J.; Payne, S. A. Expanded Phase Stability of Gd-Based Garnet Transparent Ceramic Scintillators. *J. Mater. Res.* **2014**, *29*, 2332−2337.
(13) Tyagi, M.; Meng, F.; Koschan, M.; Donnald, S. B.; Rothfuss, H.; Melcher, C. L. Effect of Codoping on Scintillation and Optical Properties of a Ce-Doped Gd3Ga3Al2O12 Scintillator. *J. Phys. D: Appl. Phys.* **2013**, *46*, 475302.
(14) Nikl, M.; Vedda, A.; Laguta, V. V. Energy Transfer and Storage Processes in Scintillators: The Role and Nature of Defects. *Radiat. Meas.* **2007**, *42*, 509−514.
(15) Selim, F. A.; Varney, C. R.; Tarun, M. C.; Rowe, M. C.; Collins, G. S.; McCluskey, M. D. Positron Lifetime Measurements of Hydrogen Passivation of Cation Vacancies in Yttrium Aluminum Oxide Garnets. *Phys. Rev. B: Condens. Matter Mater. Phys.* **2013**, *88*, 174102.
(16) Nikl, M.; Babin, V.; Mares, J. A.; Kamada, K.; Kurosawa, S.; Yoshikawa, A.; Tous, J.; Houzvicka, J.; Blazek, K. The Role of Cerium Variable Charge State in the Luminescence and Scintillation Mechanism in Complex Oxide Scintillators: The Effect of Air Annealing. *J. Lumin.* **2016**, *169*, 539.
(17) Varney, C. R.; Reda, S. M.; Mackay, D. T.; Rowe, M. C.; Selim, F. A. Strong Visible and near Infrared Luminescence in Undoped YAG Single Crystals. *AIP Adv.* **2011**, *1*, 042170.
(18) Shiran, N.; Gektin, A.; Gridin, S.; Nesterkina, V.; Vasyukov, S.; Zelenskaya, O. Defect-Controlled Scintillation Process in Undoped Y 3 Al 5 O 12 Crystals. *IEEE Trans. Nucl. Sci.* **2018**, *65*, 871−876.
(19) Stanek, C. R.; McClellan, K. J.; Levy, M. R.; Grimes, R. W. Extrinsic Defect Structure of RE3Al5O12 Garnets. *Phys. Status Solidi B* **2006**, *243*, R75.
(20) Kamada, K.; Nikl, M.; Kurosawa, S.; Beitlerova, A.; Nagura, A.; Shoji, Y.; Pejchal, J.; Ohashi, Y.; Yokota, Y.; Yoshikawa, A. Alkali Earth Co-Doping Effects on Luminescence and Scintillation Properties of Ce Doped Gd 3 Al 2 Ga 3 O 12 Scintillator. *Opt. Mater. (Amsterdam, Neth.)* **2015**, *41*, 63−66.
(21) Lucchini, M. T.; Babin, V.; Bohacek, P.; Gundacker, S.; Kamada, K.; Nikl, M.; Petrosyan, A.; Yoshikawa, A.; Auffray, E. Effect of Mg2+ Ions Co-Doping on Timing Performance and Radiation Tolerance of Cerium Doped Gd3Al2Ga3O12 Crystals. *Nucl. Instrum. Methods Phys. Res., Sect. A* **2016**, *816*, 176−183.
(22) Meng, F.; Koschan, M.; Melcher, C. L.; Cohen, P. Sintered Pellets: A Simple and Cost Effective Method to Predict the Performance of GGAG: Ce Single Crystals. *Mater. Sci. Eng., B* **2015**, *193*, 20−26.
(23) Baccaro, S.; Cecilia, A.; Mihokova, E.; Nikl, M.; Nejezchleb, K.; Blazek, K. Influence of Si-Codoping on YAG: Ce Scintillation Characteristics. *IEEE Trans. Nucl. Sci.* **2005**, *52*, 1105−1108.
(24) Zhou, X.; Luo, X.; Wu, B.; Jiang, S.; Li, L.; Luo, X.; Pang, Y. The Broad Emission at 785 Nm in YAG: Ce3+, Cr3+ Phosphor. *Spectrochim. Acta, Part A* **2018**, *190*, 76−80.
(25) Zorenko, Y.; Gorbenko, V.; Voznyak, T.; Batentschuk, M.; Osvet, A.; Winnacker, A. Luminescence of Mn2+ Ions in Tb3Al5O12 Garnet. *J. Lumin.* **2010**, *130*, 380−386.
(26) Liu, Y.; Zhang, X.; Hao, Z.; Wang, X.; Zhang, J. Tunable Full-Color-Emitting Ca 3 Sc 2 Si 3 O 12: Ce 3+, Mn 2+ Phosphor via Charge Compensation and Energy Transfer. *Chem. Commun.* **2011**, *47*, 10677−10679.
(27) Kučera, M.; Nikl, M.; Hanuš, M.; Onderišinová, Z. Gd3+ to Ce3+ Energy Transfer in Multi-component GdLuAG and GdYAG Garnet Scintillators. *Phys. Status Solidi RRL* **2013**, *7*, 571−574.
(28) Lecoq, P.; Korzhik, M. New Inorganic Scintillation Materials Development for Medical Imaging. *IEEE Trans. Nucl. Sci.* **2002**, *49*, 1651−1654.
(29) Drozdowski, W.; Brylew, K.; Witkowski, M. E.; Wojtowicz, A. J.; Solarz, P.; Kamada, K.; Yoshikawa, A. Studies of Light Yield as a Function of Temperature and Low Temperature Thermoluminescence of Gd3Al2Ga3O12: Ce Scintillator Crystals. *Opt. Mater. (Amsterdam, Neth.)* **2014**, *36*, 1665−1669.
(30) Khanin, V. M.; Rodnyi, P. A.; Wieczorek, H.; Ronda, C. R. Electron Traps in Gd3Ga3Al2O12:Ce Garnets Doped with Rare-Earth Ions. *Tech. Phys. Lett.* **2017**, *43*, 439−442.
(31) Ueda, J.; Hashimoto, A.; Takemura, S.; Ogasawara, K.; Dorenbos, P.; Tanabe, S. Vacuum Referred Binding Energy of 3d Transition Metal Ions for Persistent and Photostimulated Luminescence Phosphors of Cerium-Doped Garnets. *J. Lumin.* **2017**, *192*, 371−375.
(32) Khanin, V.; Venevtsev, I.; Rodnyi, P.; Ronda, C. Changes in Trap Parameters in Various Mixed Oxide Garnets. *Radiat. Meas.* **2016**, *90*, 104−108.
(33) Dorenbos, P. Electronic Structure and Optical Properties of the Lanthanide Activated RE3 (Al1- XGax) 5O12 (RE= Gd, Y, Lu) Garnet Compounds. *J. Lumin.* **2013**, *134*, 310−318.
(34) Khanin, V.; Venevtsev, I.; Spoor, S.; Boerekamp, J.; van Dongen, A. M.; Wieczorek, H.; Chernenko, K.; Buettner, D.; Ronda, C.; Rodnyi, P. A New Method for Unambiguous Determination of Trap Parameters from Afterglow and TSL Curves Connection: Example on Garnets. *Opt. Mater. (Amsterdam, Neth.)* **2017**, *72*, 161−168.
(35) Binet, L.; Gourier, D. Origin of the Blue Luminescence of β-Ga2O3. *J. Phys. Chem. Solids* **1998**, *59*, 1241−1249.
(36) Walsh, C. G.; Donegan, J. F.; Glynn, T. J.; Morgan, G. P.; Imbusch, G. F.; Remeika, J. P. Luminescence from β-Ga2O3: Cr3+. *J. Lumin.* **1988**, *40*, 103−104.
(37) Blahuta, S.; Bessiere, A.; Viana, B.; Dorenbos, P.; Ouspenski, V. Evidence and Consequences of Ce $\hat{}${4+} $ in LYSO: Ce, Ca and LYSO: Ce, Mg Single Crystals for Medical Imaging Applications. *IEEE Trans. Nucl. Sci.* **2013**, *60*, 3134−3141.
(38) Wu, Y.; Luo, J.; Nikl, M.; Ren, G. Origin of Improved Scintillation Efficiency in (Lu, Gd) 3 (Ga, Al) 5O12: Ce Multicomponent Garnets: An X-Ray Absorption near Edge Spectroscopy Study. *APL Mater.* **2014**, *2*, 012101.
(39) Khanin, V. M.; Vrubel, I. I.; Polozkov, R. G.; Venevtsev, I. D.; Rodnyi, P. A.; Tukhvatulina, T.; Chernenko, K.; Drozdowski, W.; Witkowski, M. E.; Makowski, M.; Dorogin, E. V.; Rudin, N. V.; Ronda, C.; Wieczorek, H.; Boerekamp, J.; Spoor, S.; Shelykh, I. A.; Meijerink, A. Complex Garnets: Microscopic Parameters Characterizing Afterglow. *J. Phys. Chem. C* **2019**, *123*, 22725.
(40) Nakamura, R.; Ueda, S. Fluorescent Material, Scintillator Using Same, and Radiation Detector Using Same. EP2157153A1, April 2013.
(41) Wang, W.; Tang, J.; Hsu, S. T. V.; Wang, J.; Sullivan, B. P. Energy Transfer and Enriched Emission Spectrum in Cr and Ce Co-Doped Y3Al5O12 Yellow Phosphors. *Chem. Phys. Lett.* **2008**, *457*, 103−105.
(42) Ueda, J.; Dorenbos, P.; Bos, A. J. J.; Kuroishi, K.; Tanabe, S. Control of Electron Transfer between Ce 3+ and Cr 3+ in the Y 3 Al 5- x Ga x O 12 Host via Conduction Band Engineering. *J. Mater. Chem. C* **2015**, *3*, 5642−5651.
(43) Blasse, G.; Bril, A. A New Phosphor for Flying-spot Cathode-ray Tubes for Color Television: Yellow-emitting Y3Al5O12-Ce3+. *Appl. Phys. Lett.* **1967**, *11*, 53−55.
(44) Kushida, T. Energy Transfer and Cooperative Optical Transitions in Rare-Earth Doped Inorganic Materials. I. Transition Probability Calculation. *J. Phys. Soc. Jpn.* **1973**, *34*, 1318−1326.
(45) Kück, S.; Hartung, S.; Hurling, S.; Petermann, K.; Huber, G. Optical Transitions in Mn 3+-Doped Garnets. *Phys. Rev. B: Condens. Matter Mater. Phys.* **1998**, *57*, 2203.
(46) Petermann, K.; Huber, G. Broad Band Fluorescence of Transition Metal Doped Garnets and Tungstates. *J. Lumin.* **1984**, *31*, 71−77.

https://dx.doi.org/10.1021/acs.cgd.9b01660
Cryst. Growth Des. 2020, 20, 3007−3017

(47) O'donnell, K. P.; Marshall, A.; Yamaga, M.; Henderson, B.; Cockayne, B. Vibronic Structure in the Photoluminescence Spectrum of Cr3+ Ions in Garnets. *J. Lumin.* **1989**, *42*, 365−373.
(48) Grinberg, M. 2E→ 4A2 Fluorescence of Cr3+ in High and Intermediate Field Garnets. *J. Lumin.* **1993**, *54*, 369−382.
(49) Henderson, B.; Marshall, A.; Yamaga, M.; O'Donnell, K. P.; Cockayne, B. The Temperature Dependence of Cr3+ Photoluminescence in Some Garnet Crystals. *J. Phys. C: Solid State Phys.* **1988**, *21*, 6187.

https://dx.doi.org/10.1021/acs.cgd.9b01660
Cryst. Growth Des. 2020, 20, 3007−3017